RESEARCH ARTICLE

steel research international

www.steel-research.de

Laser Powder Bed Fusion and Heat Treatment of the Martensitic Age-Hardenable Steel (1.2709)

Keyur Solanki, Chirag Shah, Carolin Zinn, Dirk Lehmhus, Nikhil Gupta, and Axel von Hehl*

The primary objective of this study is to clarify the fundamental question of whether, in principle, it is possible to dispense with a prior solution annealing process in favor of a direct aging heat treatment for specimens of maraging stainless steel grade X3NiCoMoTi18-9-5 (1.2709) produced by laser powder bed fusion (LPBF). The waiver of a solution annealing process would significantly increase the process efficiency and thus support a sustainable and resource-friendly production of such components. Therefore, the hardness, microstructure, and the present phases of specimens in as-built + aged condition (AB + A) and solution-annealed + aged (SOL + A) are examined during this study. Initially, an extended parameter study is performed using a Renishaw AM 250 LPBF system equipped with a pulsed mode laser system to achieve the highest possible apparent density. As test specimens, small cubes are produced for parameter study and are analyzed for porosity by means of optical microscopy. To investigate the relationship between microstructure and hardness in different material states, one series of specimens is aged directly after LPBF processing in the as-built state (AB + A). For comparison, the other series was solution annealed at 820 °C for 60 min, quenched in water and then aged (SOL + A). A maximum hardness value of 614 HV1.0 is achieved for specimen aged at 490 °C for 120 min in as built condition (AB + A), while 624 HV1.0 was measured for specimen aged at 490 °C for 180 min in conventionally solution annealed + aged (SOL + A) condition. Significant austenite reversion is not observed at aging temperature of 490 °C in both cases. Aging of specimens at temperatures of 540 and 600 °C resulted in reduction of specimen hardness due to higher percentage of austenite reversion. No significant difference between the hardness values of AB + A and SOL + A specimens is observed. It can therefore be concluded that, in principle, conventional solution annealing and ageing can be dispensed with in favor of direct aging. However, as the results are based on small sized specimens, further investigations into the scalability are needed.

1. Introduction

Laser powder bed fusion (LPBF) is a powder bed-based layer-wise additive manufacturing process where a 3D part is produced directly from a CAD model.[1] The layer-wise manufacturing process makes it possible to build parts with complex geometry without the need for complex tools or fixtures.[2] This unique manufacturing process has shown potential to process materials that have been difficult to handle with conventional manufacturing. LPBF has been used to process materials such as Inconel 718,[3–6] low carbon steels,[1,7–11] aluminum alloys,[2,12–14] stainless steel,[15,16] or titanium.[17–19] Maraging steels are ultra-low carbon, high strength Fe-Ni alloys mainly used for aerospace and tooling applications. Maraging refers to the precipitation hardening by aging of the supersaturated martensite matrix commonly found in such steels.[20] Carbon is kept low in these steels as it acts as an impurity element. The absence of carbon provides a good combination of strength, toughness, hardenability, formability,[20] and resistance to stress cracks after a heat treatment, which conventionally consists of solution annealing followed by short-term aging. Nickel is known to stabilize the austenite phase and prevent it from transforming into ferrite or pearlite during cooling. The high nickel content promotes formation of austenite, which upon rapid cooling, transforms into martensite (Refer **Figure 1**).

This martensite, due to its low carbon content, is comparatively soft and heavily dislocated.[20] Besides carbon, maraging steels also contain alloying elements such as titanium, aluminum, cobalt, and molybdenum which readily precipitate in the form Ni_3X where X = Ti, Mo, V, and W, on short-term aging at temperatures of 400–450 °C.[21–23] The high strength and toughness characteristics of maraging steel components is due to the aging of martensite formed by quenching from the Ni containing γ-Fe solid solution. The metastable martensitic matrix is

---

The ORCID identification number(s) for the author(s) of this article can be found under https://doi.org/10.1002/srin.202400173.

DOI: 10.1002/srin.202400173

K. Solanki, C. Shah, C. Zinn, A. von Hehl
Chair of Materials Science and Materials Testing (LMW)
Faculty IV: School of Science and Technology
Institute for Materials Engineering
University of Siegen
Paul-Bonatz-Straße 9-11, 57076 Siegen, Germany
E-mail: keyur.solanki@uni-siegen.de

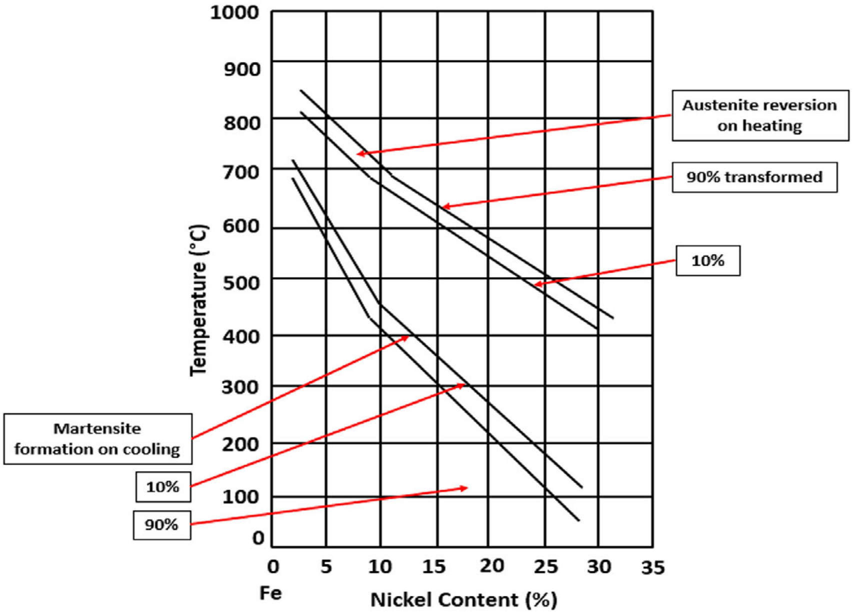

Figure 1. Meta-stable Fe-Ni phase diagram, adapted from.[26] Reproduced under the terms of the CC BY-NC-ND license. Copyright © 2017, Elsevier. Used with permission.

required to provide a high density of nucleation sites for the precipitation formation. During aging, precipitation leads to strengthening characteristics.[22] Cobalt plays an important role in this as it supports the uniform distribution of the precipitates in the martensite matrix and accelerates the precipitation process, thereby shortening the aging time.[24] Conventionally manufactured maraging steels are subjected to solution annealing to achieve a single-phase structure and induce softness to achieve machinability.[25] Subsequent aging is employed to trigger a homogeneous formation of precipitates in order to achieve the desired mechanical properties. In contrast to traditional manufacturing techniques, with LPBF, small volumes of material are selectively and sequentially melted, leading to a layer-wise consolidation of the material. Solidification and cooling rates are extremely high, reaching levels between 10^6 and $10^8\,\mathrm{K\,s^{-1}}$.[26] However, the actual material condition is not exclusively determined by high cooling rates. Once a new layer of powder is processed, the previously deposited layers experience cyclic reheating such that the intensity of the reintroduced heat reduces as the number of cycles increases.[27] Due to this cyclic reheating and quenching of the solidified track, the material undergoes an in-situ heat treatment which triggers the nucleation of hardening nanoprecipitates in the as-built condition without external aging process[26–28] which in the cast steels is expected after solution annealing followed by quenching and aging. For material processed by LPBF a refined martensitic microstructure along with higher density of nanoprecipitates and nanoparticles in an amorphous matrix was observed after aging. During aging, two phenomena occur in parallel, the first one being precipitation hardening and the second one being austenite reversion, which leads to softening. Aging at temperatures above 500 °C leads to the decomposition of the Ni_3X phase resulting in the release of Ni into the matrix, thus promoting the formation of austenite by a diffusion-controlled reaction. Preventing this conversion of martensite into austenite and ferrite is the key to achieving high hardness.[20]

The working hypothesis of the study is as follows: The extremely rapid solidification and cooling rates achieved during the LPBF process lead to a fine and a highly metastable material state with high supersaturation of alloying elements. Due to the intrinsic cyclic reheating and quenching, some of the dissolved alloying elements form precipitates in-situ while the other part remains in the solution until the end of the LPBF process. These remaining alloying elements form precipitates during the subsequent direct aging treatment so that conventional solution annealing and quenching can be waived to shorten the process chain, thus improving process efficiency and enabling sustainable production of components made from maraging steel grade 1.2709 processed via LPBF. However, failing to dissolve those precipitates already formed in situ during production might lead to their growth during direct aging, which might cancel out their strengthening effect, leading to a material condition inferior to that achieved via the full processing route including the solution heat treatment. To evaluate the interaction of these phenomena in terms of microstructure and achievable mechanical properties is the primary objective of this work.

D. Lehmhus
Department of Casting Technology and Lightweight Construction
Fraunhofer Institute for Manufacturing Technology and Advanced Materials IFAM
28359 Bremen, Germany

N. Gupta
Department of Mechanical and Aerospace Engineering
New York University
Tandon School of Engineering
New York 11201, USA

2. Experimental Section

The material, 1.2709 maraging steel, was supplied by Oerlikon Metco. The powder was prepared via argon gas atomization. The composition of the alloy is shown in **Table 1** and the general morphology of the material is shown in **Figure 2**. The particle size distribution of the powder was measured by the supplier by means of laser diffraction (ASTM C 1070). The specification sheet provided by the supplier stated that 90% of the particles did not exceed the size of 54 μm.

A Renishaw AM 250 LPBF machine was used to build the test specimens. The system was fitted with a pulsed mode Yttrium Aluminium Garnet (YAG) fiber laser system operating at a wavelength of 1064 nm. The laser emits output power periodically for a short duration at a fixed repetition rate (Refer **Figure 3**). It provides much higher peak power (P_{peak}) in comparison to the continuous wave systems,[29] which translates to higher volumetric laser energy density (E_{d}). Studies have shown that pulsed mode lasers thus have a much deeper penetration capability compared to continuous wave lasers under otherwise similar conditions of laser power, interaction time and beam diameter. Therefore, the heat input required to achieve the same penetration depth is much lower compared to continuous wave lasers. Due to the downtime between the pulses, pulsed laser systems are also beneficial to avoid issues related to heat accumulation. Average power (P_{avg}) for a pulsed laser is lower than the peak power because the laser is switched off for longer than it is switched on. The average power is the product of peak power times the duty factor, where the duty factor is the proportion of time that the laser is actively emitting laser light. Average peak power is defined as the average of the distributed power within a laser pulse.[29]

The study started with understanding the process parameters and their effect on the defects generated in the processed specimens. From the literature survey, it was evident that increasing or decreasing the volumetric laser energy density (E_{d}) affects the characteristics of the formed meltpool, leading to a change in the bonding of the material.[30] E_{d} (J mm^{-3}) was calculated as shown in Equation (2)[31]

$$v = d/t \tag{1}$$

$$E_{\text{d}} = P/(h\,v\,l) \tag{2}$$

$$R = h\,v\,l \tag{3}$$

where, P = Laser power (W), h = Hatching distance (mm), v = Scanning velocity (mm s^{-1}), l = Layer thickness (mm), d = Point distance (mm), t = Exposure time (s), E_{d} = Volumetric laser energy density (J mm^{-3}), R = Build rate (mm^3 s^{-1}).

Test cubes of size 10 × 10 × 10 mm were produced under argon atmosphere with build plate temperature set at 80 °C. Laser power of $P = 200$ W was used. Hatching distance, the distance between two consecutive laser scan lines, was kept constant at $h = 80$ μm. A meandering hatch pattern was used. After each scan, the scanning direction was rotated by Ø = 67° for the next layer. Scanning velocity (Equation (1)) is the velocity at which the laser scans the material to be processed. Layer thickness, which is the thickness of the deposited powdered material, was kept constant at $l = 40$ μm. Point distance is the distance between two consecutive laser points and exposure time is the time for which a point is exposed to the laser beam. **Figure 4** shows the schematic of process parameters considered in the experimental study.

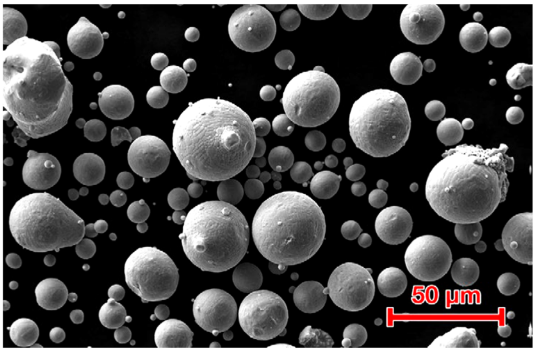

Figure 2. Morphology of the alloy powder supplied by Oerlikon Metco.

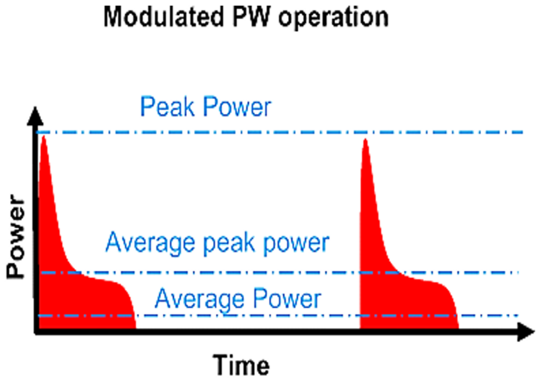

Figure 3. Schematic representation of pulsed mode (PW) laser.[29] Licensed under CC BY 4.0.

Initial parameters (shown in **Table 2**) were selected from the available literature.[22] The volumetric laser energy density was then varied between $E_{\text{d}} = 44$ J mm^{-3} and $E_{\text{d}} = 77$ J mm^{-3}. **Table 3** shows the design of experiment for the experiment series, designated as MS01, conducted to obtain highest possible apparent density of test specimens.

Post LPBF processing, the specimens were cut from the build plate by means of wire electrical discharge machining, grinded

Table 1. Chemical composition (wt%) of maraging steel 1.2709.

Elements	Fe	Ni	Co	Mo	Ti	C
Manufacturer specification	Balance	17%–19%	8.00%–10.00%	4.50%–5.50%	0.80%–1.20%	<0.03%
As tested via EDS analysis	Balance	17.7%	8.2%	5.1%	0.9%	<0.03%

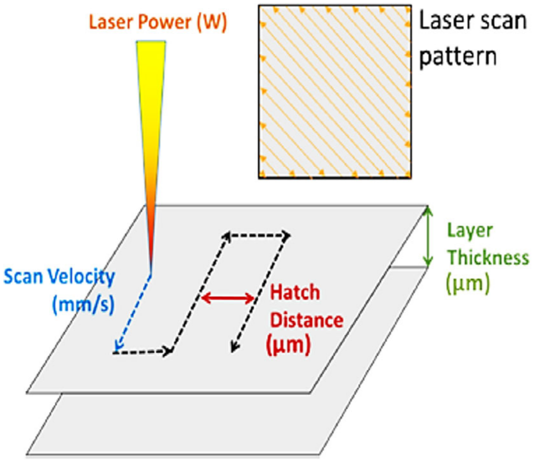

Figure 4. Schematic representation of LPBF process parameters, adapted from.[34] Licensed under CC BY 4.0.

and polished to conduct optical microscopy. Cross-sectional images were captured for a single cross section such that the cross-sectional area was perpendicular to the build direction. The area of the pores in this cross-sectional image was determined via digital image processing software (ImageJ). The apparent density (d) of specimens was then calculated as follows

$$d = \left(A_{\text{total}} - A_{\text{pore}}\right)/A_{\text{total}} \tag{4}$$

where A_{total} is the complete area of the cross-sectional area under analysis and A_{pore} is the sum of the area of all the pores.

For heat treatment, two sets of 15 specimens each were prepared. The first set was directly aged in as-built (AB + A) condition and the second set was conventionally solution annealed for 1 h at 820 °C, followed by quenching in still water and subsequently aged (SOL + A). Both AB + A and SOL + A specimen were aged at three different temperature levels of 490, 540 and 600 °C,[22] with aging times ranging between 5 and 300 min. The design of experiments is setup in such a way that lower aging times are chosen for higher aging temperatures. The three temperature values are selected because it is reported that over-aging above 500 °C accelerated the reduction of hardness values whereas over-aging below 500 °C only moderately affected hardness values.[22] The resulting test matrix is shown in **Table 4**. Hardness of the specimens was assessed via Vickers hardness tests at a load value of 1 kg on the Future Tech FV700 hardness testing system in accordance with the DIN EN ISO 6507-1 standard. Six measurements were taken at various positions across the specimen test surface.

For electron backscatter diffraction (EBSD) measurement, specimens were prepared by embedding in a conductive mold (2 volume parts of CEM3070 powder with 1 volume part of CEM3070 hardening agent supplied by CLOEREN

Table 2. Baseline set of parameters.[22]

Hatching distance (h) [mm]	Layer thickness (l) [mm]	Exposure time (t) [s]	Point distance (d) [mm]	Scan velocity (v) [mm s^{-1}]	Build rate (R) [mm^3 s^{-1}]	Volumetric laser energy density (E_d) [J mm^{-3}]
0.080	0.040	0.080	0.065	813	2.6	77

Table 3. Design of experiment for experiment series MS01.

Cube number	Hatching distance [mm]	Layer thickness [mm]	Exposure time [s]	Point distance [mm]	Scan velocity [mm s^{-1}]	Build rate [mm^3 s^{-1}]	Volumetric laser energy density [J mm^{-3}]
1	0.080	0.040	80	0.065	813	2.6	77
2			123	0.100			
3			185	0.150			
4			246	0.200			
5			50	0.050	1000	3.2	63
6			100	0.100			
7			150	0.150			
8			200	0.200			
9			42	0.050	1200	3.8	52
10			83	0.100			
11			125	0.150			
12			167	0.200			
13			210	0.200	952	3.0	66
14				0.250	1190		53
15				0.180	857		73
16				0.300	1429		44

Table 4. Design of experiment for heat treatment process evaluation.

Aging temperature [°C]	Aging time [min]				
490	60	120	180	240	300
540	15	30	60	120	180
600	5	10	15	30	60

TECHNOLOGY GmbH) and grinded with sandpaper size from 300 grit to 4000 grit followed by polishing steps of 0.5 and 0.25 μm diamond suspension followed by 3 h of vibratory polishing. The specimens were then examined on Helios Nanolab 600 Scanning Electron Microscope by FEI in a vacuum atmosphere at acceleration voltage $V_{acc} = 20$ kV and at current $I = 5.5$ nA.

3. Results and Discussions

3.1. Parameter Optimization and Apparent Density

Figure 5 shows the processed specimens and their positions on the build plate. The specimen numbers in Figure 5 correspond to the specimen numbers in Table 3. The apparent density of the specimens is shown in **Table 5**.

Cube 1 was processed with baseline parameters.[22] An apparent density of 99.90% was obtained for cube 13 processed with tweaked parameters at volumetric laser energy density of 66 J mm^{-3}. Cubes 14 and 16 were processed with volumetric laser energy densities of 53 and 44 J mm^{-3} respectively. **Figure 6** and **7** show the effect of laser power and scanning velocity on the nature of porosities formed. As volumetric laser energy density is a function of laser power and scanning velocity, the combination of these two parameters plays a key role in staying within an optimum operating window. A lower value of volumetric laser energy density results in a lack of fusion defects whereas a higher value results in balling defects and keyhole porosities.[31] In Figure 6, it is evident that with lower volumetric laser energy densities, porosity reduced with a maximum apparent density of 99.90% achieved at $E_d = 66$ J mm^{-3}. The irregularly shaped pores in Figure 7 suggest a lack of fusion due to poor melting of powder at higher scanning velocities. The area marked in red also shows poor adhesion with the substrate (the black arrow next to the figures indicates build direction).

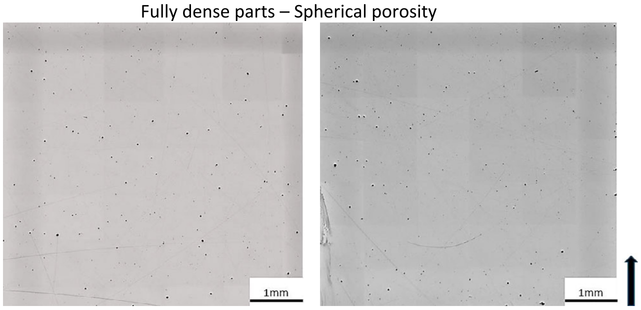

Cube 1
Apparent Density: 99.88%
Volumetric Laser Energy Density: 77 J mm^{-3}

Cube 13
Apparent Density: 99.90%
Volumetric Laser Energy Density: 66 J mm^{-3}

Figure 6. Effect of laser power and scanning velocity on the formation of porosities. Fully dense specimens with spherical/gas porosity. The arrow shows the build direction.

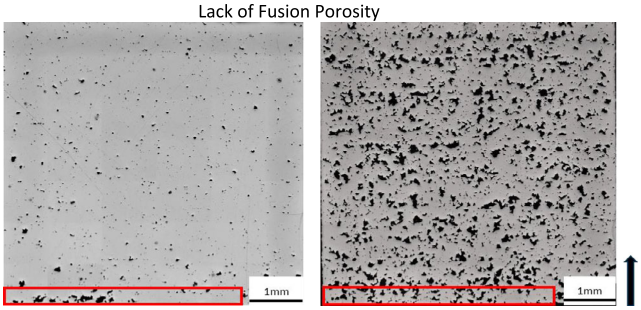

Cube 14
Apparent Density: 98.80%
Volumetric Laser Energy Density: 53 J mm^{-3}

Cube 16
Apparent Density: 86.44%
Volumetric Laser Energy Density: 44 J mm^{-3}

Figure 7. Effect of laser power and scanning velocity on the formation of porosities. Less dense specimens with lack of fusion porosity. The arrow shows the build direction.

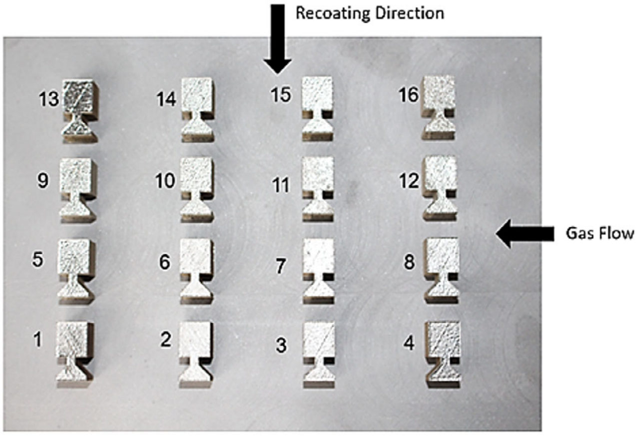

Figure 5. Processed specimens on the build plate.

Table 5. Apparent density (*d*, %) and volumetric laser energy density (E_d, J mm^{-3}) of cubes from experiment series MS01.

Cube number	1	2	3	4	5	6	7	8	9	10	11	12	13	14	15	16
E_d [J mm^{-3}]	77				63				52				66	53	73	44
d [%]	99.88	99.85	99.82	99.68	99.61	99.74	99.60	99.14	97.09	99.13	98.33	97.78	99.90	98.80	99.85	86.44

3.2. Microstructure, EBSD Phase Maps and Hardness

Figure 8a shows an optical image of the as-built specimen depicting the formed meltpools. The specimens were etched with solutions according to Kalling and Klemm to make the microstructure visible. Figure 8b depicts the microstructure of the cube in as-built condition etched with Kalling solution. Columnar grains and fine microstructure can be observed which are characteristics of high cooling gradient during LPBF processing. Figure 8c shows microstructure of the cube etched with Klemm solution after solution annealing. A coarse grained microstructure is observed after solution annealing which could be due to the driving force to reduce energy of the thermodynamic system. This coarse structure (area highlighted in red in Figure 8b,c) is referred as martensite packets which consist of fine and parallel heavy dislocated laths.[22,32]

For hardness measurement, the cubes were grinded, polished, and subjected to Vickers hardness measurements.

At aging temperatures of 490 °C (Refer **Figure 9**a) and 540 °C (Refer Figure 9b), there was no considerable drop in hardness values. The hardness distribution in Figure 9b and in Figure 9c depict a conventional strength-aging curve such that peak hardness could have been achieved when there was an optimum distribution of coherent and semi-coherent particles. However, at aging temperatures of 600 °C (Refer Figure 9c), a measurable drop in hardness is observed at higher aging times. Further investigation for specimens in solution annealed + aged condition at 600 °C was not performed as the hardness of the specimens in as-built + aged condition was already quite low.

This steep reduction in hardness could be attributed to the breaking down or growth of intermetallic precipitates and the reversion of martensite to austenite.[19,21] EBSD phase scans for specimen in AB + A and SOL + A condition aged at 490 °C (Refer **Figure 10**a,c,e) show that with increasing aging time, the average grain size increases (from 3.1 to 4.2 μm in AB + A condition and 5.8 μm in SOL + A condition), however, the increase in the volume percentage of reversed austenite is negligible. A similar trend in the average grain size can be observed in EBSD scans for specimen in AB + A and SOL + A condition aged at 540 °C (Refer Figure 10g,i,k), but with a higher percentage of reversed austenite. At 600 °C, after just 60 min of aging, 11 vol.% of reversed austenite is observed (Refer Figure 10r). Reversion to austenite takes place in maraging steel at every aging temperature. However, higher temperatures as well as extended aging times accelerate both the disintegration of precipitates and the conversion of martensite to austenite, thus reducing the specimen hardness.[19] In literature, Molybdenum is also shown to facilitate the reversion rate of

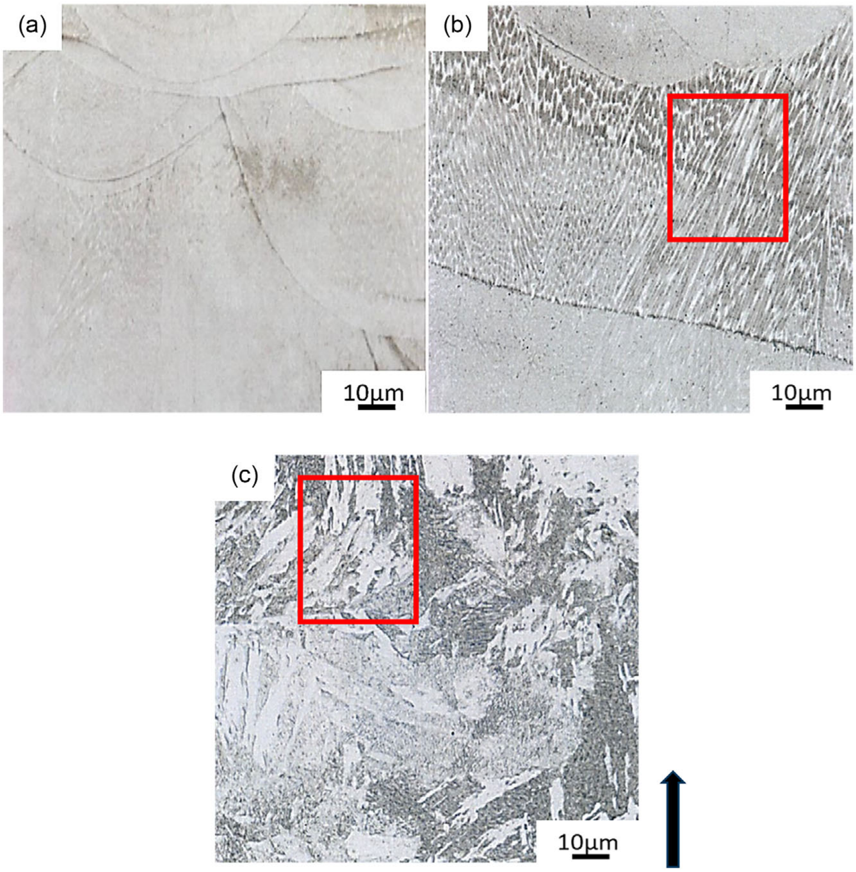

Figure 8. Optical images: a) Optical image of as-built (AB) specimen showing formed melt pools; b) Microstructure of as-built (AB) specimen showing elongated grains; c) Microstructure of solution annealed (SOL) specimen showing coarse grains. The arrow identifies the build direction for all optical images.

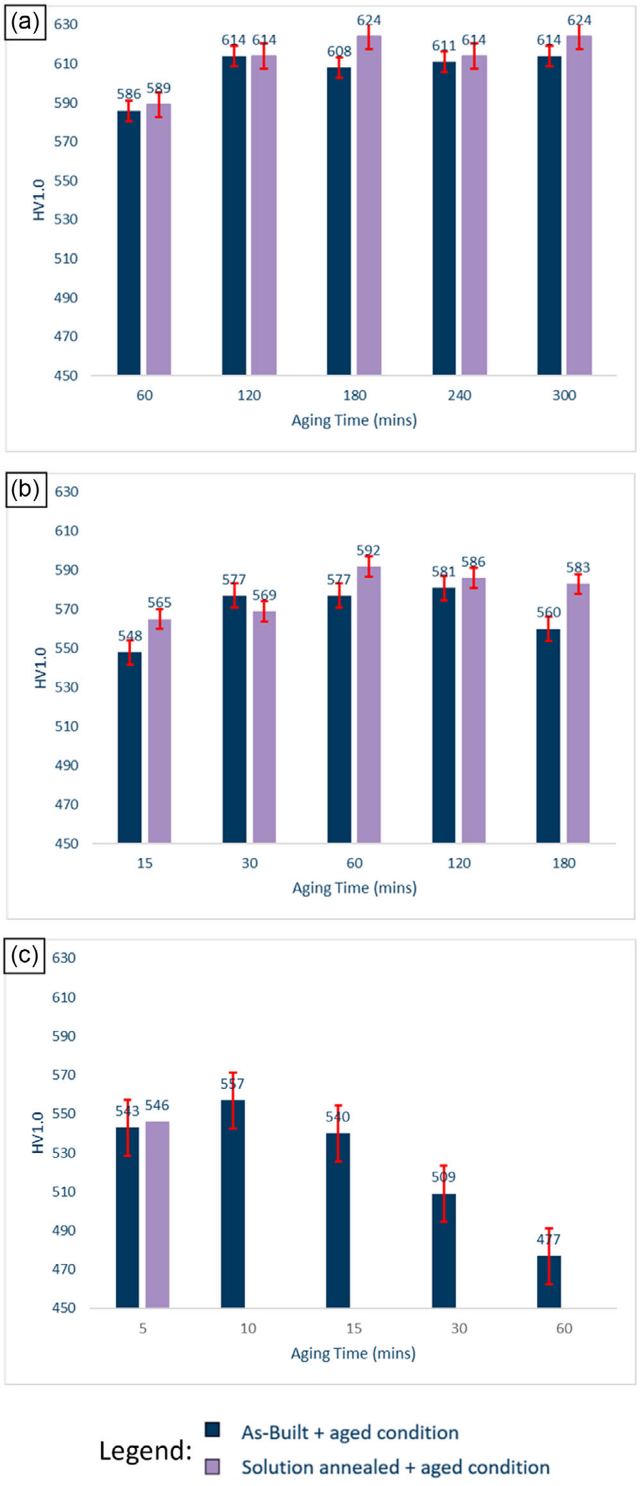

Figure 9. Maximum specimen hardness (HV1.0) values: a) specimen aged at 490 °C; b)specimen aged at 540 °C; and c) specimen aged at 600 °C.

martensite to austenite by promoting the formation of Fe_2Mo which results in local enrichment of Ni in the matrix.[33] Thus, due to diffusion controlled reaction, at higher temperatures, austenite is obtained. From the phase scans, it can be seen that at lower aging temperatures (490 and 540 °C) the reversed austenite is scattered at cell boundaries. At high aging temperature (600 °C) the reversed austenite is observed at the intracellular level. The inverse pole figures do depict preferred orientations for sample aged at 490 °C for 120 min [111] (Refer Figure 10a), for sample aged at 600 °C for 5 min [111] (Refer Figure 10m) and for sample aged at 600 °C for 30 min [111] (Refer Figure 10o). However, the difference between the minimum and the maximum intensity in the scale presented in all the IPF figures is quite narrow to really differentiate between regions of preferred orientation and random orientation. It is therefore inferred from the IPF figures that there is no preferred orientation (build direction: [001]).

4. Conclusions

A research study was undertaken to investigate the relationship between microstructure and hardness in different material states of 1.2709 maraging steel, focusing on the question of whether direct aging following specimen production would lead to mechanical properties matching those of solution heat treated, then aged samples. The objective was to establish a basis for a shortening of process chains for this type of alloy. To this end, a batch of small sized cubes was produced by LPBF and divided into two series. One series was aged directly after LPBF process in the as-built state (AB + A). For comparison, the other series was aged after conventional solution annealing and quenching (SOL + A). The main conclusions of this research can be summarized as follows: 1) Volumetric laser energy density was found to be the main parameter controlling porosity levels. 99.90% specimen density (apparent) was achieved at 66 J mm^{-3} of volumetric laser energy density; 2) Max. hardness values of 614 HV1.0 was obtained after direct aging of the as-built specimens at 490 °C for 120 min; 3) Max. hardness values of 624 HV1.0 was obtained after aging of previously conventionally solution treated and quenched (SOL + A) specimens at 490 °C for 180 min; 4) No significant difference between the hardness values of AB + A and SOL + A specimens was observed; and 5) Aging at temperatures above 540 °C lead to steep a reduction in hardness values due to high amount of austenite reversion.

The investigation was focused on the clarification of the fundamental question of whether, in principle, it is possible to dispense with a prior conventional solution annealing and quenching in favor of a direct aging treatment of 1.2709 maraging steel, which can be confirmed by the gained results. Since the primary aim of this study was to clarify the fundamental question of whether it is possible in principle to dispense with conventional heat treatment in favour of direct ageing heat treatment for maraging steels of grade X3NiCoMoTi18-9-5 (1.2709) after processing using LPBF, the material characterization was initially limited to the investigation of simple cubes produced at density optimized process parameters. Hence, there are a couple of open research questions. Among others, the influence of the build plate temperature hasn't been addressed yet. Furthermore, since only simple cubes were examined, the scalability to real component sizes and geometries, which influence the locally time-dependent temperature development

Aging temperature: 490°C, Aging time: 120 minutes, Specimen condition: As-built + Aged (AB+A)

Aging temperature: 490°C, Aging time: 180 minutes, Specimen condition: As-built + Aged (AB+A)

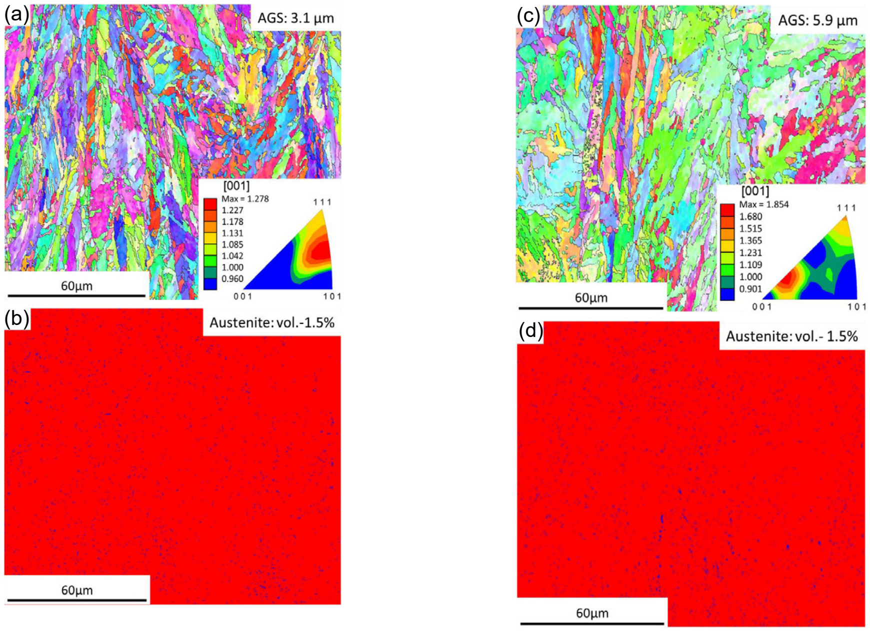

Aging temperature: 490°C, Aging time: 180 minutes, Specimen condition: Solution annealed + Aged (SOL+A)

Aging temperature: 540°C, Aging time: 120 minutes, Specimen condition: As-built + Aged (AB+A)

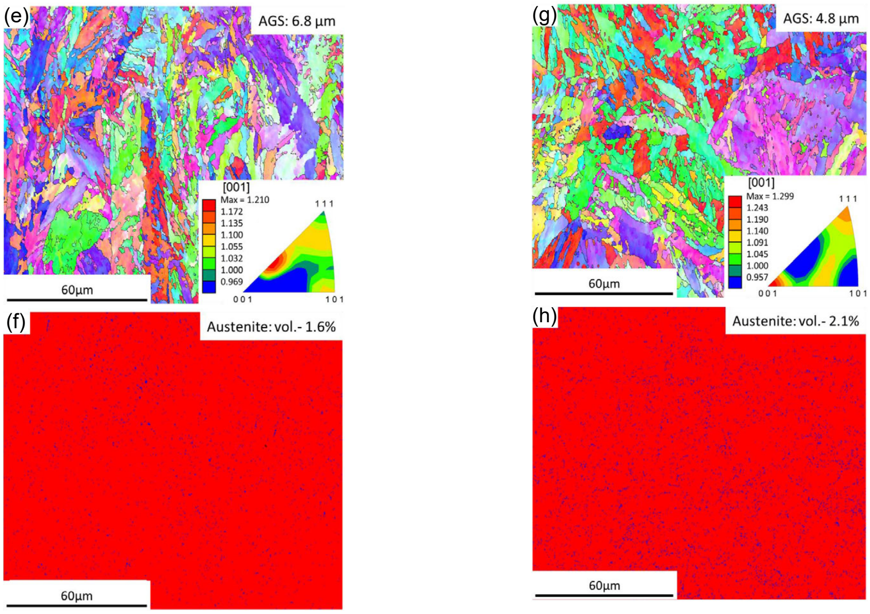

Figure 10. EBSD mapping with inverse pole figure (IPF) and phase scan showing average grain size and percentage of retained austenite. The percentage of austenite in the phase scans is shown as volume percentage (vol.%) for all scans. a) EBSD mapping of specimen aged at 490 °C in as-built + aged condition for 120 min, b) Phase scan for specimen aged at 490 °C in as-built + aged condition for 120 min, c) EBSD mapping of specimen aged at 490 °C in as-built + aged condition for 180 min, d) Phase scan for specimen aged at 490 °C in as-built + aged condition for 180 min, e) EBSD mapping of specimen aged at 490 °C in solution annealed + aged condition for 180 min, f) Phase scan for specimen aged at 490 °C in solution annealed + aged condition for 180 min, g) EBSD mapping of specimen aged at 540 °C in as-built + aged condition for 120 min, h) Phase scan for specimen aged at 540 °C in as-built + aged condition for 120 min, i) EBSD mapping of specimen aged at 540 °C in as-built + aged condition for 180 min, j) Phase scan for specimen aged at 540 °C in as-built + aged condition for 180 min, k) EBSD mapping of specimen aged at 540 °C in solution annealed + aged condition for 180 min, l) Phase scan for specimen aged at 540 °C in solution annealed + aged condition for 180 min, m) EBSD mapping of specimen aged at 600 °C in as-built + aged condition for 5 min, n) Phase scan for specimen aged at 600 °C in as-built + aged condition for 5 min, o) EBSD mapping of specimen aged at 600 °C in as-built + aged condition for 30 min, p) Phase scan for specimen aged at 600 °C in as-built + aged condition for 30 min, q) EBSD mapping of specimen aged at 600 °C in as-built + aged condition for 60 min, r) Phase scan for specimen aged at 600 °C in as-built + aged condition for 60 min. The arrow indicates build direction and holds true for all scans.

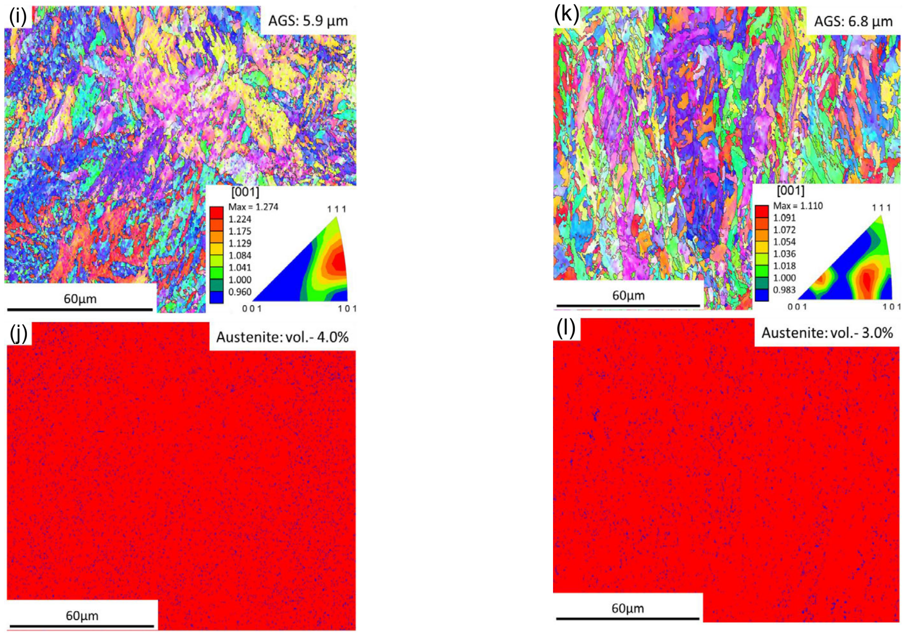
Aging temperature: 540°C, Aging time: 180 minutes, Specimen condition: As-built + Aged (AB+A)

Aging temperature: 540°C, Aging time: 180 minutes, Specimen condition: Solution annealed + Aged (SOL+A)

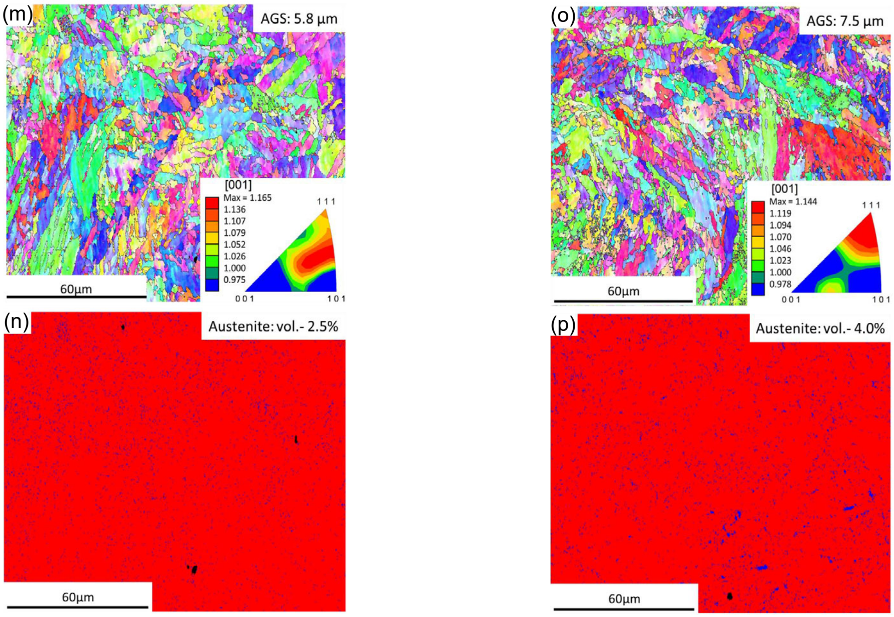
Aging temperature: 600°C, Aging time: 5 minutes, Specimen condition: As-built + Aged (AB+A)

Aging temperature: 600°C, Aging time: 30 minutes, Specimen condition: As-built + Aged (AB+A)

Figure 10. Continued.

and thus, as a hypothesis, the local supersaturation conditions for the subsequent direct aging, needs to be investigated in more detail. Therefore, the next step will be to produce and test material samples for the quasi-static tensile test and for service life investigations on the basis of the results obtained. In addition, detailed investigations of the solution state after the LPBF will be carried out by mapping the chemical composition using TEM/EDS and supplemented by calorimetric analyses of the precipitation development during aging and Austenite reversion.

Aging temperature: 600°C, Aging time: 60 minutes, Specimen condition: As-built + Aged (AB+A)

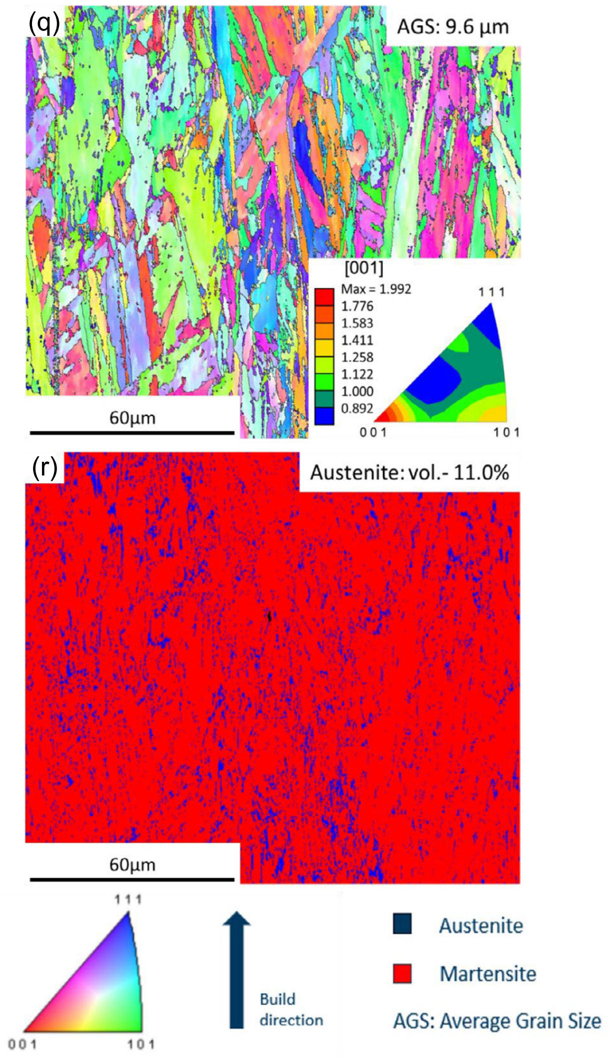

Figure 10. Continued.

Acknowledgements

The authors would like to acknowledge Leibniz IWT, University of Bremen, NYU Tandon School of Engineering and Materialise GmbH for providing the opportunity. The authors also thank our colleagues Mr. Tim Domagala (Materialise GmbH), Mr. Tim Steghofer, Ms. Lena Heemann and Mr. Daniel Knoop at Leibniz IWT for their support in conducting the necessary experiments and the interpretation of the results. A part of this work was performed at the Micro- and Nanoanalytics Facility (MNaF) of the University of Siegen. The research was supported and funded by the MAPEX Institute of Materials and Processes at University of Bremen along with the Santander BISIP scholarship offered through the research collaboration of University of Bremen and NYU Tandon School of Engineering. N.G. thanks NSF CMMI-2036802 for partial support of this work. [Correction added on 2 July 2024, after first online publication: Figure 9 in-text citation is changed to Figure 5 in the sentence "The specimen numbers in Figure 9 correspond to the specimen numbers in Table 3."]

Open Access funding enabled and organized by Projekt DEAL.

Conflict of Interest

The authors declare no conflict of interest.

Data Availability Statement

The data that support the findings of this study are available from the corresponding author upon reasonable request.

Keywords

aging behavior, laser powder bed fusion, maraging steel, parameter optimization

Received: February 28, 2024
Revised: May 29, 2024
Published online: June 27, 2024

---

[1] K. Kempen, E. Yasa, L. Thijs, J.-P. Kruth, J. van Humbeeck, *Phys. Proc.* **2011**, *12*, 255.

[2] F. Calignano, D. Manfredi, E. P. Ambrosio, L. Iuliano, P. Fino, *Int. J. Adv. Manuf. Technol.* **2013**, *67*, 2743.

[3] P. Karimi, T. Raza, J. Andersson, L.-E. Svensson, *Int. J. Adv. Manuf. Technol.* **2018**, *94*, 2199.

[4] P. L. Blackwell, *J. Mater. Process. Technol.* **2005**, *170*, 240.

[5] Z. Wang, K. Guan, M. Gao, X. Li, X. Chen, X. Zeng, *J. Alloys Compd.* **2012**, *513*, 518.

[6] Q. Jia, D. Gu, *Opt. Laser Technol.*, **2014**, *62*, 161.

[7] Z. Guo, W. Sha, D. Li, *Mater. Sci. Eng.*, **2004**, *373*, 10.

[8] J. Damon, T. Hanemann, S. Dietrich, G. Graf, K.-H. Lang, V. Schulze, *Int. J. Fatigue* **2019**, *127*, 395.

[9] S. Bodziak, K. S. Al-Rubaie, L. D. Valentina, F. H. Lafratta, E. C. Santos, A. M. Zanatta, Y. Chen, *Mater. Charact.* **2019**, *151*, 73.

[10] D. Croccolo, M. de Agostinis, S. Fini, G. Olmi, F. Robusto, S. Ćirić-Kostić, S. Morača, N. Bogojević, *Fatigue Fract. Eng. Mater. Struct.* **2019**, *42*, 374.

[11] F. F. Conde, J. D. Escobar, J. P. Oliveira, M. Béreš, A. L. Jardini, W. W. Bose, J. A. Avila, *Mater. Sci. Eng.* **2019**, *758*, 192.

[12] D. Lehmhus, T. Rahn, A. Struss, P. Gromzig, T. Wischeropp, H. Becker, *Materials* **2022**, *15*, 7386.

[13] M. Joo, in *New Trends in Technologies: Devices, Computer, Communication and Industrial Systems*, Sciyo, Rijeka **2010**.

[14] M. Krishnan, E. Atzeni, R. Canali, F. Calignano, D. Manfredi, E. P. Ambrosio, L. Iuliano, *Rapid Prototyping J.* **2014**, *20*, 449.

[15] R. Brandt, F. Walther, J. T. Sehrt, D. Biermann, M. Lindner, F. Stern, T. Grimm, S. Hase, M. Tilger, *Sci. Technol. Adv. Mater.* **2022**, *2*, 38.

[16] Z. Sun, B. Sun, V. Soh, C. Lee, D. Lau, F. Wei, A. K. D. Silva, M. Lin, C. C. Tan, P. Wang, U. Ramamurty, *Acta Mater.* **2024**, *263*, 119534.

[17] S. Ghouse, S. Babu, R. J. van Arkel, K. Nai, P. A. Hooper, J. R. Jeffers, , *Mater. Des.*, **2017**, *131*, 498.

[18] W. Xu, M. Brandt, S. Sun, J. Elambasseril, Q. Liu, K. Latham, K. Xia, M. Qian, *Acta Mater.* **2015**, *85*, 74.

[19] H. Gong, K. Rafi, H. Gu, T. Starr, B. Stucker, *Addit. Manuf.* **2014**, *1–4*, 87.

[20] W. Sha, Z. Guo, in *Maraging Steels*, Woodhead Publishing, Sawston, UK **2009**.

[21] G. Casalino, S. L. Campanelli, N. Contuzzi, A. D. Ludovico, *Opt. Laser Technol.* **2015**, *65*, 151.

[22] R. Casati, J. N. Lemke, A. Tuissi, M. Vedani, *Metals* **2016**, *6*, 218.

[23] X. Mei, Y. Yan, L. Qiao, *Acta Mater.* **2023**, *256*, 119141.

[24] A. P. Mouritz, in *Introduction to Aerospace Materials*, Woodhead Publishing, Sawston, UK **2012**.
[25] R. Singh, in *Applied Welding Engineering*, 2nd ed., Butterworth-Heinemann, Oxford **2016**.
[26] C. Tan, K. Zhou, W. Ma, P. Zhang, M. Liu, T. Kuang, *Mater. Des.* **2017**, *134*, 23.
[27] S. Amirabdollahian, F. Deirmina, L. Harris, R. Siriki, M. Pellizzari, P. Bosetti, A. Molinari, *Scr. Mater.* **2021**, *201*, 113973.
[28] P. Kürnsteiner, M. B. Wilms, A. Weisheit, P. Barriobero-Vila, E. A. Jägle, D. Raabe, *Acta Mater.* **2017**, *129*, 52.
[29] J. Coroado, S. Ganguly, W. Suder, S. Williams, S. Meco, G. Pardal, *Int. J. Adv. Manuf. Technol.* **2021**, *115*, 2929.
[30] I. Yadroitsev, I. Yadroitsava, P. Bertrand, I. Smurov, *Rapid Prototyping J.* **2012**, *18*, 201.
[31] Karimi, P., Master's Thesis, University West (Trollhätten, Sweden), **2016**.
[32] M. Opiela, G. Fojt-Dymara, A. Grajcar, W. Borek, *Materials* **2020**, *13*, 1489.
[33] C. Shamantha, R. Narayanan, K. Iyer, V. Radhakrishnan, S. Seshadri, S. Sundararajan, S. Sundaresan, *Mater. Sci. Eng.* **2000**, *287*, 43.
[34] J. P. Oliveira, A. D. LaLonde, J. Ma, *Mater. Des.* **2020**, *193*, 108762.